Supporting Information

Supplement 1

The lithography and metallization methods used constrain the maximum thin film thickness that could be obtained for defining the initial thin film slices. Poor edge fidelity present in the slice edges following the metal lift–off step limited the maximum thin film thickness to approximately 30nm. Beyond h=30nm, the edge roughness approached a value greater than 20nm. Edge roughness on this order of magnitude could potentially translate to the liquid rivulet upon PLiD producing an undesired perturbation in the rivulet. As a result, the aspect ratio (height/width) for the initial varicose slices was limited to relatively small h/w ratios.

It is also important to note that such a small h/w ratio could have potentially left the liquid retraction step susceptible to, for example, instabilities of spinodal or even 'pearling' type discussed in some detail in reference [18] The successful formation of the rivulet morphology for the film thickness and thin film strip width combinations presented in this paper demonstrate a successful process niche located between lithography constraints and other destabilizing forces.

Supplement 2

It has been demonstrate that the cumulative liquid lifetime ($n*\tau_L$) produced by multiple (n) laser pulses yields the same morphology as a single laser pulse equal to the cumulative melt time [1]. Moreover, the rapid heating and cooling rates leave negligible time for morphological relaxation mechanisms such as diffusion, oxidation, etc. As a result, it was possible to image the dewetting dynamics at various stages during both the transport and instability growth stages by multiple iterations of laser pulsing and SEM imaging. As an example, figure 1c shows several images at an intermediate step in the self–assembly process where the rivulet morphology has developed and surface perturbations are evident on the rivulet surface.

The liquid lifetime controls the available hydrodynamic transport time per laser pulse, *defined here as the time during which the entire Ni thin film thickness is liquefied*, therefore excluding time periods of partial liquefaction. Simulations of the time–temperature evolution of a Ni thin film supported on a silicon substrate revealed liquid lifetimes of 7.5ns and 14.9ns when using a laser fluence of 380 mJ/cm^2 and 420 mJ/cm^2, respectively (figure 1). The details of this simulation, based on [4,31-33] are described below

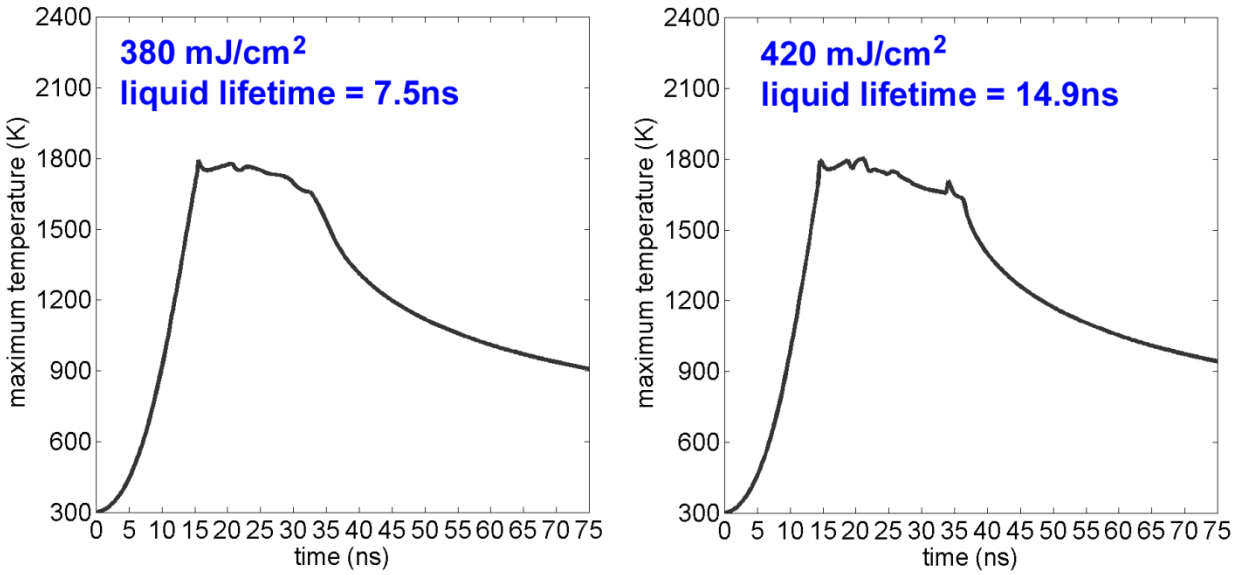

Figure S2_1 Liquid lifetime of the Ni thin film as a function of laser fluence.

The temperature profile in the nickel and silicon layers was estimated as a function of depth (*z*) and time (*t*) by simulating the one–dimensional heat equation, including a source term *I(z,t)* in order to account for the absorbed portion of the incident pulsed laser photon source;

$$\rho(z)\cdot c_p(z)\cdot\frac{\partial T(z,t)}{\partial t}=\frac{\partial}{\partial z}\cdot\left(k(z)\cdot\frac{\partial T(z,t)}{\partial z}\right)-I(z,t) \quad (5)$$

Material properties such as the density $\rho(z)$, heat capacity $c_p(z)$ and thermal conductivity $k(z)$ are represented with a z–dependence in equation (5) in order to account for material change across the nickel (Ni) thin film – silicon (Si) substrate boundary. Table 1 below lists the values of the variables mentioned in this Supplement. The source term included (1) a Gaussian approximation for the photon time pulse and considered (2) the liquid and solid phase reflectivity *R(t)* as well as the real refractive index (*n*) and extinction coefficient (*k*) of both the Ni and Si layers

$$I(z,t)=\frac{2\cdot(1-R(t))\cdot E_d(t)\cdot\alpha(z,t)}{\tau_{FWHM}}\cdot\sqrt{\frac{ln2}{\pi}}\cdot e^{-\alpha(z,t)\cdot z}\cdot e^{-\frac{4ln2\cdot(t-t_0)^2}{(\tau_{FWHM})^2}} \quad (6)$$

where $E_d(t)$ is the time–dependent laser fluence (J/m^2), $\alpha(z,t)$ is the absorption coefficient (equation 7) and τ_{FWHM} is the full width at half maximum of the laser pulse. The absorption coefficient is given as;

$$\alpha(z,t)=\frac{4\pi\cdot n\cdot k}{\lambda} \quad (7)$$

where λ is the laser wavelength. The reflectivity of either the solid or liquid phase may be derived from the real refractive index and the extinction coefficient by;

$$R(z=0,t)=\frac{(n-1)^2+k^2}{(n+1)^2+k^2} \quad (8)$$

The velocity of the solid–liquid interface was estimated assuming that nucleation dynamics governed the speed of propagation [31,33] due to the rapid melting and resolidification processes that take place during nanosecond, pulsed laser irradiation. The interface velocity is dictated by the magnitude of the undercooling of the melt and/or overheating of the solid according to;

$$V(z,t)_i = V_o \cdot \left[1 - e^{-\frac{L(z)}{c_p \cdot T_m(z)} \cdot \frac{T_i(z,t)-T_m(z)}{T_i(z,t)}}\right] \quad (9)$$

where V_o is the interface limit velocity, $L(z)$ is the latent heat of fusion, $T_m(z)$ is the melting temperature, $T_i(z,t)$ is the interface temperature and $V(z,t)_i$ is the solid–liquid interface velocity. The phase change initiated at the Ni thin film surface and propagated into the simulation domain with time. The explicit finite difference method was used to estimate the time evolution of the temperature spatial profile. The stability criteria represented in equation (10) was maintained during the simulation

$$\frac{\Delta t \cdot k(z)_{max}}{c_p(z)_{min} \cdot \rho(z)_{min} \cdot \Delta z(z)_{min}} \leq 0.5 \quad (10)$$

where Δt is the simulation time step and $\Delta z(z)$ is the depth dependent spatial discretization. A variable spatial grid size is used to increase efficiency. In the film itself, we use small $\Delta z_{surface}$=1nm, Since the computational domain itself has to be relatively large in order to prevent the constant temperature boundary (300K) from affecting the solution, we use progressively larger $\Delta z(z)$ as we move away from the surface, reaching the maximum value of 200nm at 25 microns below the solid/film interface. More precisely, the boundary conditions that we use are

$$\left.\frac{\partial T(0,t)}{\partial z}\right|_{z=h} = 0 \quad (11)$$

while within the silicon substrate the boundary condition is;

$$T(25\mu m, t) = 300K \quad (12)$$

Materials Properties

	Si	Ni	
k	150	90	J/m s K
c_p	680	450	J/kg K
ρ	2300	7900	kg/m^3
L	1808	336	kJ/kg
T_m	1410	1453	K
V_o	312	500	m/s
n	1.5	(1.4,2.1)	
k	3.6	(2.1,3.3)	

Laser & Simulation Properties

λ	248	nm
E_d	380, 420	mJ/cm^2
τ_{FWHM}	18	ns
t_o	18	ns
z_{max}	25	μm
Δz_{min}	1	nm
Δz_{max}	0.2	μm
Δt	2.5	fs
t_{max}	75	ns
T_o	300	K
h_{Ni}	23	nm

Table 1 Ni and Si materials properties along with the pulsed laser heating simulation parameters. Entries in the table of the form (solid, liquid) represent the phase dependent values of specific properties.

Supplement 3

Fast Fourier transforms (FFT) of SEM images were calculated by the following method. First, an SEM image of a partially fragmented rivulet was converted into binary format (rivulet=1, substrate=0). A summation was then calculated in the transaxial dimension of the resulting binary image (i.e. perpendicular to the cylindrical axis). The 1D FFT of the resulting data vector was then calculated. The resulting FFT was displayed as a spectrum of Fourier components (A_n) vs. mode wavelength (λ). The FFT was found to provide an estimate of the amplitude distribution on the rivulet surface and was directly compared to the modified Rayleigh–Plateau dispersion curve.

Supplement 4

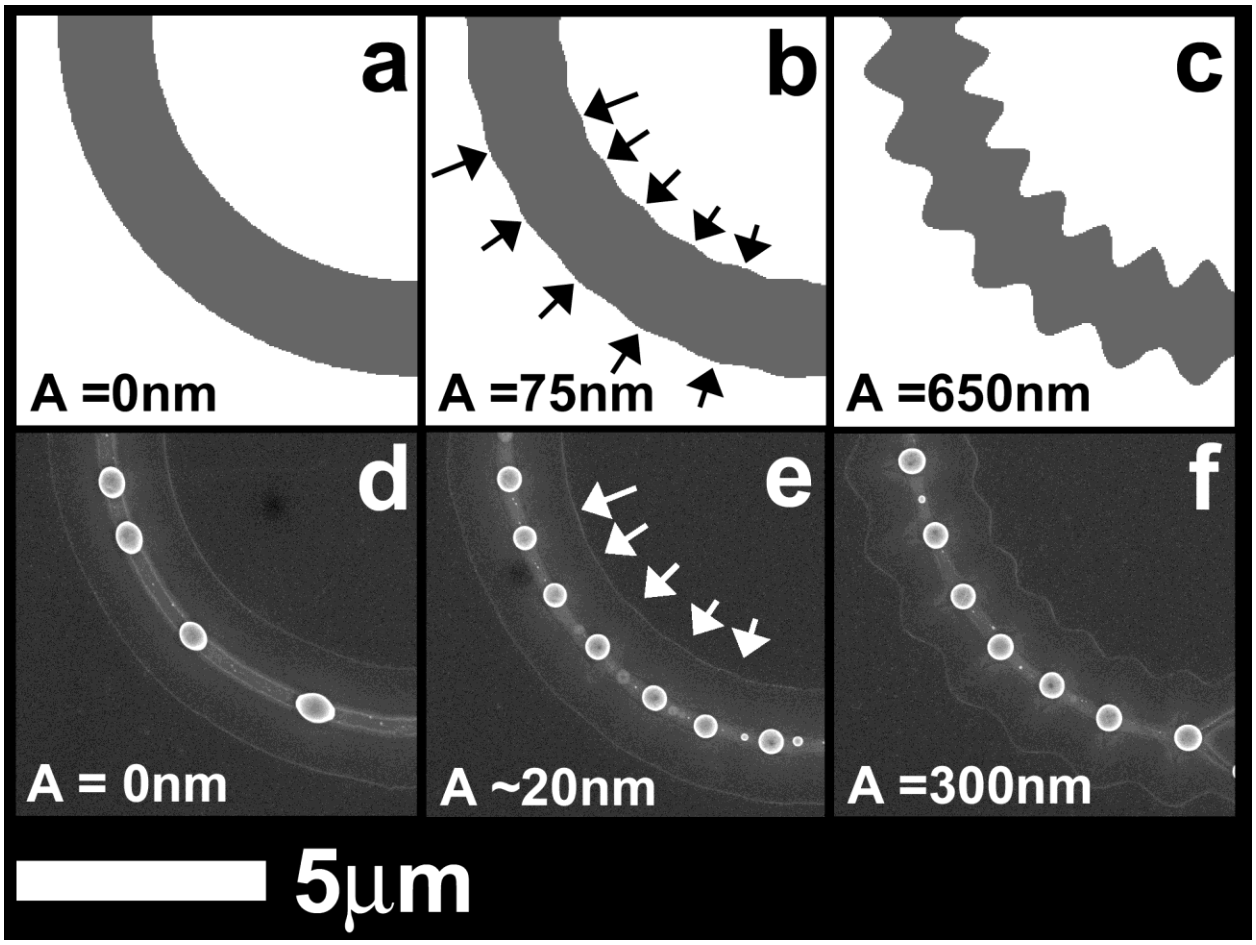

Figure S4_1 Even minute sinusoidal nanoscale perturbations lead to nanoparticle assembly. Figures (a–c) show the computer aided design (CAD) for one quarter of a thin film annulus where the synthetic amplitude (A_o) is variable among the three designs. In a) no synthetic perturbation has been imposed on the thin film annulus edge in the CAD. In b) and c) an unstable, synthetic perturbation with an average wavelength of 1.352μm has been imposed on the thin film annulus edge where A_o=75nm and 650nm for b) and c), respectively. SEM images are displayed in (d–f) for the complementary Ni thin film annuli, resulting from the CAD in figures (a–c), irradiated with 20pulses at 380 mJ/cm^2. These irradiation conditions are sufficient to induce both rivulet formation and nanodroplet formation. The thin film annulus thickness was 23nm±1.2nm and the average width was 1.87μm±12nm for all cases. Edge lines of secondary electron contrast demarcate the original thin film annuli edge and geometry in (d–f). Due to proximity effects during the electron beam facilitated, pattern exposure process the actual widths of the annuli are larger when compared with the design. In addition, the design amplitude is reduced in the actual thin film annulus. For example, the initial perturbation in (e) is ~20nm. This amplitude is on the order of the image pixel size making it difficult to even resolve the perturbation at this particular image

magnification. Therefore, the location of the peaks have been identified in the CAD in (b) using arrow features and these arrows were then superimposed over the complementary SEM image in (e) in order to aid the reader in discerning their positions in (e). The nanoparticle positions and pitch correspond with the location of the unstable synthetic amplitude peak positions in the CAD and the synthetic amplitude, respectively. The SEM image in (f) has been provided for the reader to clearly discern the oscillation peaks and troughs in the design – although the amplitude in the thin film annulus shown in (f) is larger, the phase of the ring amplitude is the same is in (e). The correlation in particle positions between the two images further demonstrates the correlation in initial perturbation phase.

Supplement 5

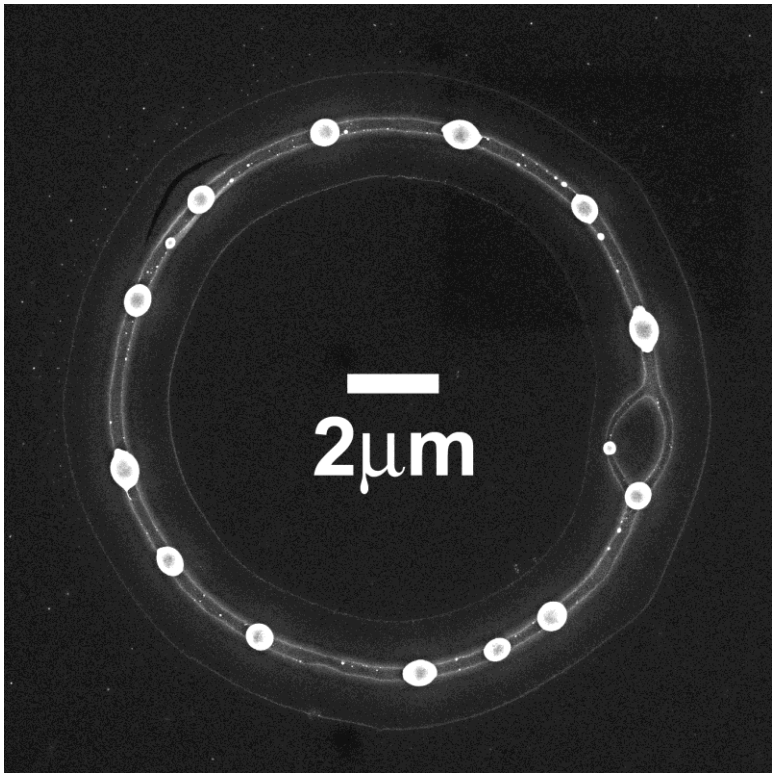

Figure S5_1 An SEM image of the nanoparticle morphology produced after the application of 20 laser pulses (E_d = 380 mJ/cm^2) to a smooth Ni annulus. The visible annular artifact in the image demarcates the outline of the thin film annulus prior to dewetting. The average pitch, as well as the standard deviation in pitch, are approximately the same as that obtained for a thin film annulus with a 820nm synthetic perturbation (see figure 3d).

Supplement 6

The simulations are carried out by numerically solving the equation (3). The simulations are based on spatially discretizing the equation (3) using finite difference, and then carrying out the time evolution using the implicit Crank-Nicolson method, as described in detail elsewhere[34]. The initial condition is a thin film strip with smooth boundaries and periodic boundary conditions in the longitudinal direction. The initial thin film strip is then perturbed by varicose perturbations as discussed in the main text. The substrate itself is assumed to be pre–wetted by an ultrathin, equilibrium Ni film the thickness of which was determined by computing the value of Hamaker's constant based on a separate set of experiments involving breakup of a Ni film of uniform thickness as discussed in our earlier work [24].